

# Compressible turbulent convection in highly stratified adiabatic background

John Panickacheril John,<sup>1†</sup> and Jörg Schumacher<sup>1,2</sup>

<sup>1</sup>Institut für Thermo- und Fluidodynamik, Technische Universität Ilmenau, Postfach 100565, D-98684 Ilmenau, Germany

<sup>2</sup>Tandon School of Engineering, New York University, New York City, New York 11201, USA

(Received xx; revised xx; accepted xx)

Buoyancy-driven turbulent convection leads to a fully compressible flow with a strong top-down asymmetry of first- and second-order statistics when the adiabatic equilibrium profiles of temperature, density and pressure decay very strongly across the convection layer. The growth of this asymmetry and the formation of an increasingly thicker stabilized sublayer with a negative mean convective heat flux at the top of the convection zone is reported here by a series highly resolved three-dimensional direct numerical simulations beyond the Oberbeck-Boussinesq and anelastic limits for dimensionless dissipation numbers  $0.1 \leq D \leq 0.8$  at fixed Rayleigh number  $Ra = 10^6$  and superadiabaticity. The highly stratified compressible convection regime appears for  $D > D_{\text{crit}} \approx 0.65$ , when density fluctuations collapse to those of pressure; it is characterized by an up to nearly 50% reduced global turbulent heat transfer and a sparse network of focused thin thermal plumes falling through the top sublayer deep into the bulk.

**Key words:** Compressible turbulent convection

---

## 1. Introduction

Solar convection close to the surface proceeds in the presence of an extremely stratified adiabatic background equilibrium which is characterized by scale heights, the distances across which temperature  $T$ , density  $\rho$ , or pressure  $p$  drop by an order of magnitude, as small as  $\ell \sim 10^3$  km amounting to only 5‰ of the total depth of the solar convection layer,  $H \sim 2 \times 10^5$  km (Christensen-Dalsgaard 2002; Nordlund *et al.* 2009; Schumacher & Sreenivasan 2020). It is one prominent example for a fully compressible convection flow which is highly asymmetric when up- and down-welling thermal plumes are compared. Driven by the strong radiative cooling at the top surface, cold plasma sinks into the interior with nearly the speed of sound at the narrow edges of the granules, the convection cells in the solar case. Plasma rises moderately to the surface across the granule interior with a typical diameter of about  $10^3$  km (Magic *et al.* 2013). It is yet open, how deep the narrow plumes reach into the highly stratified interior (Cossette & Rast 2016; Brandenburg 2016; Anders *et al.* 2019) and how much they get focused by compressibility effects to overcome turbulent dispersion. Answers to these questions would also provide insights on the vertical extent of supergranules, the larger-scale convection cells in the background with an extension of about 30 granule diameters (Rincon & Rieutord 2018; Hanson *et al.* 2020) and on the related *solar conundrum* of anomalously low velocity

† Email address for correspondence: john.panickacheril-john@tu-ilmenau.de

fluctuation amplitudes from helioseismology in comparison to models (Hanasoge *et al.* 2012). All this sets the physical motivation for the present study.

In this work, we want to study fully compressible convection in the presence of highly stratified adiabatic equilibrium profiles for  $T$ ,  $\rho$ , and  $p$ . We thus analyse a series of direct numerical simulations (DNS) towards the high stratification limit of  $D \rightarrow 1$  for the dissipation number  $D$  (defined below). Our goal is to analyse the genuine compressibility effects isolated from complex multi-physics, as in the solar example above, and from temperature dependencies of dynamic viscosity and thermal conductivity. Our three-dimensional DNS beyond the Oberbeck-Boussinesq (Chillà & Schumacher 2012) and anelastic regimes (Ogura & Phillips 1962; Verhoeven *et al.* 2015; Jones *et al.* 2022) lead to strongly differing boundary layer dynamics at the top and bottom, such as a sublayer formation at the top with mean negative convective heat flux which causes a reduction of the global turbulent heat transfer by almost 50% for  $D = 0.8$ . In this layer, narrow focused thermal plumes form at the top and fall deeply into the highly stratified bulk of the layer. Our study thus demonstrates that some typical phenomena in natural convection flows can be understood in significantly simpler compressible flow configurations even though being far away from the natural flow case in terms of Rayleigh and Prandtl numbers.

## 2. Simulation model and parameters of compressible convection

The equations of motion for compressible convection are given by

$$\partial_t \rho + \partial_i(\rho u_i) = 0, \quad (2.1)$$

$$\partial_t(\rho u_i) + \partial_j(\rho u_i u_j) = -\partial_i p + \partial_j \sigma_{ij} + \rho g \delta_{i,3}, \quad (2.2)$$

$$\partial_t(\rho e) + \partial_j(\rho e u_j) = -p \partial_i u_i + \partial_i(k \partial_i T) + \sigma_{ij} S_{ij}, \quad (2.3)$$

$$p = \rho R T \quad \text{where} \quad R = C_p - C_v. \quad (2.4)$$

These equations correspond to mass, momentum and energy conservation laws along with the ideal gas equation of state. Here,  $\rho$ ,  $\rho u_i$ ,  $p$ ,  $\rho e$ ,  $T$  are the mass density, momentum density components, pressure, internal energy density, and temperature, respectively. The viscous stress tensor is  $\boldsymbol{\sigma} = 2\mu \boldsymbol{S} + 2\mu \boldsymbol{I}(\boldsymbol{\nabla} \cdot \boldsymbol{u})/3$  with the Kronecker tensor  $\boldsymbol{I}$  and the rate of strain tensor  $\boldsymbol{S} = (\boldsymbol{\nabla} \boldsymbol{u} + \boldsymbol{\nabla} \boldsymbol{u}^T)/2$ . The dynamic viscosity  $\mu$  is assumed to be constant in these simulations. The thermal conductivity  $k$  is related to the viscosity through the Prandtl number,  $k = \mu C_p / Pr$ . In our DNS,  $Pr = 0.7$ .  $C_p$  and  $C_v$  correspond to specific heat at constant pressure and volume, respectively. Their ratio,  $\gamma = C_p / C_v = 1.4$  for a diatomic gas.

A uniform grid is used in  $x$ - and  $y$ -directions along with periodic boundary conditions. In wall-normal  $z$ -direction, a non-uniform grid with a point clustering near the walls which follows a hyperbolic tangent stretching function. Spatial derivatives are calculated by a 6th-order compact scheme (Lele 1992) for all points except near the walls (Baranwal *et al.* 2022); there 4th- and 3rd-order compact schemes are used at the last two grid points near the wall. No-slip, isothermal boundary conditions are applied at the top and bottom. The boundary condition for  $p$  is evaluated using the  $z$ -component of the momentum equation at  $z = 0, H$ ,  $\partial p / \partial z = \partial \sigma_{iz} / \partial x_i + \rho g$ . The fields are advanced in time by a low storage 3rd-order Runge-Kutta with a Courant number of  $CFL = 0.5$ .

Incompressible Rayleigh-Bénard convection is determined by the Rayleigh and Prandtl numbers,  $Ra$  and  $Pr$ . In compressible convection, additional dimensionless parameters need to be introduced. The first one is the *dissipation number*  $D$  given by

$$D = \frac{gH}{C_p T^B}. \quad (2.5)$$

Case	$D$	$T_a^B/T_a^T$	$\rho_a^B/\rho_a^T$	$M_t^{\max}$	$Nu$	$Re$	$\lambda_{\rho_{\min}}$	$\delta_{u_z T}$	$(\lambda_{\rho'^T}, \delta_{\rho'^T})$	Style
1	0.10	1.10	1.3	0.14	$7.94 \pm 0.05$	$424 \pm 2$	0.002	0.001	(0.001, 0)	
2	0.34	1.52	2.8	0.32	$7.64 \pm 0.01$	$414 \pm 1$	0.012	0.005	(0.006, 0.012)	
3	0.50	2.00	5.7	0.41	$6.93 \pm 0.02$	$407 \pm 2$	0.024	0.010	(0.012, 0.024)	
4	0.60	2.50	9.9	0.49	$6.24 \pm 0.01$	$370 \pm 8$	0.037	0.016	(0.018, 0.037)	
5	0.65	2.86	13.8	0.55	$5.90 \pm 0.01$	$364 \pm 2$	0.042	0.019	(0.021, 0.042)	
6	0.70	3.33	20.3	0.54	$5.80 \pm 0.04$	$425 \pm 2$	0.051	0.023	(0.023, 0.051)	
7	0.75	4.00	32.0	0.60	$5.14 \pm 0.01$	$399 \pm 0$	0.068	0.033	(0.028, 0.068)	
8	0.80	5.00	55.9	0.61	$4.46 \pm 0.03$	$356 \pm 1$	0.098	0.051	(0.035, 0.098)	

TABLE 1. List of the direct numerical simulations. All cases have  $Pr = 0.7$ ,  $Ra \approx 10^6$ ,  $\epsilon = 0.1$ ,  $\gamma = C_p/C_v = 1.4$ , and an aspect ratio,  $\Gamma = L/H = 4$  resolved by  $N_x : N_y : N_z = 512 : 512 : 256$  grid points. We list dissipation number  $D$ , ratios of adiabatic temperatures and densities from bottom to top, the global maximum turbulent Mach number  $M_t^{\max}$ , the Nusselt and Reynolds numbers,  $Nu$  and  $Re$ . The statistical error/difference for the Nusselt number and Reynolds number are less than 2% for all cases. Furthermore, we display boundary layer scales for density, convective heat flux, and density-temperature correlations. In all figures that follow, coloured lines are given as in this table.

The parameter  $D$  can be considered as a rescaled dry adiabatic lapse rate as it determines differences in the thermodynamic properties across the layer depth in a purely isentropic process. The adiabatic temperature ratio between top (T) and bottom (B) is  $T_a^T/T_a^B = (1 - D)$ , the corresponding density ratio follows to  $\rho_a^T/\rho_a^B = [T_a^T/T_a^B]^{1/(\gamma-1)}$ . The subscript "a" corresponds to the adiabatic equilibrium without convection. In order to initiate convective motion, the actual temperature gradient across the layer must be greater than due to a purely adiabatic process (Jeffreys 1930), i.e.,  $T^B - T^T > T_a^B - T_a^T$ . In our study, the bottom plate is taken as the reference, thus  $T^B = T_a^B$  is a constant for all cases; the instability criterion reduces to  $T^T < T_a^T$ .

The second compressible parameter is the *superadiabaticity*  $\epsilon$ , which is given by

$$\epsilon = \frac{T_a^T - T^T}{T_B}. \quad (2.6)$$

Superadiabaticity is the excess relative temperature gradient with respect to the adiabatic equilibrium state, or in other words, a measure of the driving of convection. If one takes the characteristic free-fall velocity,  $U_f = \sqrt{\epsilon g H}$ , then a free-fall Mach number,

$$M_f(z) = \frac{U_f}{\gamma R \langle T(z) \rangle_{A,t}} = \sqrt{\frac{\epsilon D}{\gamma - 1}} \sqrt{\frac{T_B}{\langle T(z) \rangle_{A,t}}}, \quad (2.7)$$

follows. Thus strength of compressibility is thus a function of both,  $\epsilon$  and  $D$ . From (2.7), it is expected that compressibility at the top is higher than at the bottom. For  $\epsilon \rightarrow 0$ , we get the anelastic approximation where the acoustic waves are filtered out from the equations. Rayleigh Bérnard convection in the Oberbeck-Boussinesq (OB) regime follows for  $\epsilon, D \rightarrow 0$ . On the basis of the new parameters, we will use  $Ra = \epsilon g H^3 / (\nu \kappa)$  and Prandtl number,  $Pr = \nu / \kappa$ , where  $\kappa$  is the temperature diffusivity and  $\nu = \mu / \rho$  the kinematic viscosity. In this work, we focus on a constant and low but finite superadiabaticity,  $\epsilon = 0.1$  for a range of  $D$  from 0.1 to 0.8. All other governing parameters such as the  $Ra$ ,  $Pr$  and aspect ratio,  $\Gamma$  are kept constant, see Table. 1. In all figures that follow, unless specified otherwise, we use the plotting style given in the last column.

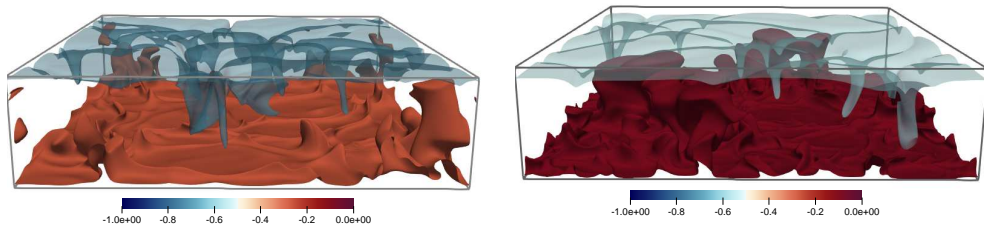


FIGURE 1. Snapshots of the normalized superadiabatic temperature fields. Isosurfaces of normalized  $T_{sa}$  for case 1 with  $D = 0.1$  (left) and case 8 with  $D = 0.8$  (right) are shown. The right panel shows a ridge network with thin thermal plumes emanating from the top deeply into the convection layer. The superadiabatic temperature is normalized in both panels to  $[-1, 0]$ . (Left) Contour levels at the bottom and top correspond to  $-0.27$  and  $-0.73$ , respectively. The bottom and top contours to the right stand for  $-0.09$  and  $-0.61$ , respectively, see the color bars.

### 3. Growing asymmetry with increased stratification

The adiabatic temperature profile,  $T_a(z) = T_a^B(1 - Dz)$ , is the equilibrium profile. Thus the part of temperature corresponding to convection is the superadiabatic temperature defined as

$$T_{sa}(\mathbf{x}, t) = T(\mathbf{x}, t) - T_a(z). \quad (3.1)$$

In figure 1, we compare the contour visualization of  $T_{sa}$  for the two extreme cases in our series with  $D = 0.1$  (low) and  $D = 0.8$  (high). The left panel corresponds to case 1, closest to the OB limit. Not surprisingly, the plumes from the top and bottom are more or less symmetric in shape and frequency. However, this top-bottom-symmetry disappears completely for case 8 in the right panel. One observes broader thick plumes from the bottom compared to a network of slender thinner plumes originating from the top. Recently, John & Schumacher (2023) showed that thinner plumes from the top boundary are a common characteristic of compressible convection regardless of the relative boundary layer thickness, but here the differences are very pronounced.

Similar asymmetry is observed for the mean profile of the superadiabatic temperature,  $\langle T_{sa}(z) \rangle_{A,t}$ , where the notation  $\langle \cdot \rangle_{A,t}$  corresponds to an average over the horizontal directions and time. In figure 2(a), we plot the normalized superadiabatic temperature,  $\langle T_{sa}(z) \rangle_{A,t} / \Delta \langle T_{sa} \rangle_{A,t}$  as a function of depth  $z$  where  $\Delta \langle T_{sa} \rangle_{A,t} = \langle T_{sa}(z=0) \rangle_{A,t} - \langle T_{sa}(z=H) \rangle_{A,t}$ . Clearly one observes that the asymmetry increases considerably with growing dissipation number. As  $D$  increases, the bulk temperature is increasingly closer to the bottom temperature. It is also evident from the figure that the thermal boundary layer thickness at the top is large in comparison to that at the bottom as  $D$  increases. We can quantify this thickness as the mean of a *local* thermal boundary layer thickness (Scheel & Schumacher 2014) which is given by

$$\tilde{\lambda}^{B,T}(x, y) = \frac{1}{H} |\langle T_{sa}(0, H) - T_{sa}(H/2) \rangle_{A,t}| \left| \frac{\partial \langle T_{sa} \rangle_{A,t}}{\partial z} \right|_{z=0,H}^{-1}. \quad (3.2)$$

We plot  $\lambda^{B,T} = \langle \tilde{\lambda}^{B,T} \rangle_{A,t}$  as a function of  $D$  in the inset of figure 2(a). The difference between the boundary layer thickness at the bottom and top plate increases with  $D$  in agreement with the differences observed in the distributions of the instantaneous, local thermal boundary layer thicknesses (John & Schumacher 2023). The top boundary layer

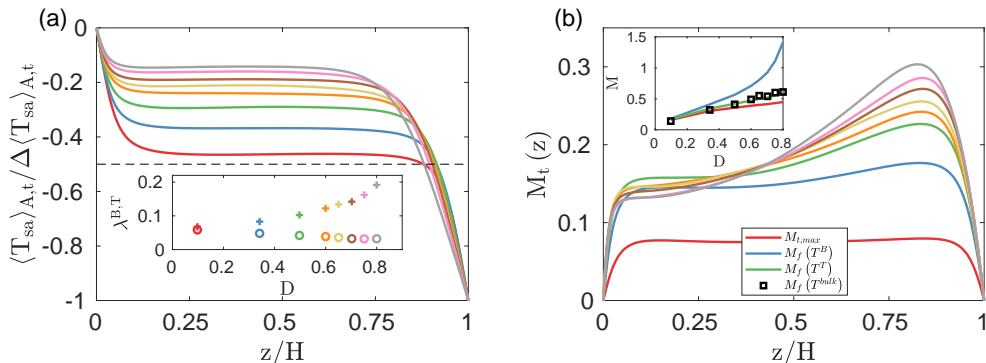


FIGURE 2. Asymmetry of the (a) normalized superadiabatic temperature and (b) the turbulent Mach number  $M_t$ . The inset in (a) corresponds to mean thermal boundary layer thickness  $\lambda^{B,T}(D)$ . Symbols + and o are for the top and bottom boundary layer thickness, respectively. The inset in (b) shows  $M_f(D)$  from (2.7). The red, blue and green lines are at  $z/H = 0, 1$ , and  $0.5$ . The black squares are the maximum Mach numbers as given Table 1, which are observed in the simulations over the whole space and time. The legend in (b) corresponds to the inset figure.

thickness increases drastically with  $D$  whereas bottom boundary layer thickness is almost invariant. This along with increased asymmetry in the bulk towards the bottom plate, as seen in the normalized  $T_{sa}$ -profiles, suggests that at high  $D$ , the mixing is not as efficient as in OB and compressibility effects are mainly localized near the top boundary.

An asymmetry similar to that of  $\langle T_{sa}(z) \rangle_{A,t}$  is observed for the turbulent Mach number too with significant localized compressibility seen near the top boundary. The turbulent Mach number is defined as

$$M_t(z) = \frac{u_{\text{rms}}(z)}{\sqrt{\gamma R \langle T(z) \rangle_{A,t}}} \quad \text{with} \quad u_{\text{rms}}(z) = \sqrt{\sum_{i=1}^3 \left[ \langle u_i^2(z) \rangle_{A,t} - \langle u_i(z) \rangle_{A,t}^2 \right]}. \quad (3.3)$$

The turbulent Mach number at the top increases monotonically with  $D$  whereas the behaviour at the bottom boundary is non-monotonic with  $D$ . At the bottom,  $M_t$  increases up to  $D = 0.5$  and then decreases with  $D$  as a result increasing the asymmetry between the boundaries further as seen in figure 2(b).

In the inset of figure 2(b), we compare the resulting maximum turbulent Mach number in the flow with the estimate from (2.7). The black squares are the maximum local turbulent Mach number for each  $D$  encompassing all time steps and spatial locations. The red and blue lines correspond to  $M_f$ -estimates using the bottom and top temperatures,  $T^B$  and  $T^T$ , respectively. One finds that the resulting maxima of  $M_t$  are in between these estimates. This is due to no-slip boundary conditions at the wall; thus the velocity peaks only at the outer layer of the boundary layer and in the bulk. Since the (mean) bulk temperature is closer to that at the bottom plate, the values of  $M_t$  are closer to  $M_f(T^B)$ . A really close agreement for the simulations is seen, when the Mach number is estimated using the bulk temperature, green line in the inset figure. This suggests that a simple estimate such as in (2.7) can give us a good idea about the level of compressibility in the flow. We would like to point out that in compressible turbulence  $M_t$  is not sufficient to characterize the system; an additional parameter  $\delta$ , the ratio of dilatational to solenoidal root mean square velocities, needs to be included as discussed in Donzis & John (2020); John *et al.* (2019, 2020, 2021).

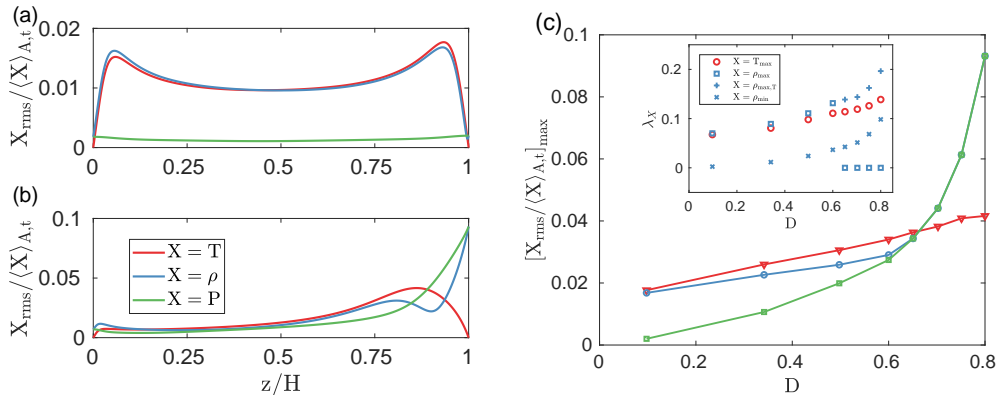


FIGURE 3. Relative fluctuations of thermodynamic quantities for (a)  $D = 0.1$  and (b)  $D = 0.8$ . (c) Maximum of the relative thermodynamic fluctuations versus dissipation number,  $D$ . For all figures, the red, blue and green correspond to temperature, density and pressure respectively. Inset of (c) shows four different distances  $\lambda_X$  as a function of  $D$ . For the definition of the specific  $\lambda_X$  we refer to the text in section 4 and the legend of the inset.

#### 4. Fluctuations of state variables and regime transition

A major consequence of compressibility are the fluctuations of  $p$ ,  $\rho$ , and  $T$ . In figure 3, we compare these fluctuations as a function of depth for the two extreme cases of our DNS series,  $D = 0.1$  and  $0.8$ . John & Schumacher (2023) showed that  $D \leq 1 - \epsilon$ , which would result in a maximally possible theoretical value of  $D = 0.9$  in our DNS series. The relative fluctuations are defined as  $X_{\text{rms}} / \langle X \rangle_{A,t}$  with  $X_{\text{rms}} = (\langle X^2 \rangle_{A,t} - \langle X \rangle_{A,t}^2)^{1/2}$ . Panel (a) at  $D = 0.1$  shows that pressure fluctuations are negligible. The magnitude of the density and temperature fluctuations are of the same order of magnitude and the profiles of both quantities are practically identical. These findings are consistent with the OB limit at  $\epsilon, D \rightarrow 0$ .

In figure 3(b), the relative fluctuations of  $p$ ,  $\rho$ , and  $T$  at  $D = 0.8$  are shown. As result of high compressibility at  $D = 0.8$  at the top, see figure 2(b) for  $M_t(z)$ , the thermodynamic fluctuations are considerably higher compared to the bottom one. Close to the top boundary, the pressure and density fluctuations dominate the temperature fluctuations. This is due to the constant temperature imposed at the boundaries which results in an isothermal condition. For an assumed ideal gas,  $p \propto \rho$ . Indeed this is evident for  $D = 0.8$  at the top boundary as the relative fluctuations of density and pressure perfectly match at the top boundary. This would be also true at bottom boundary and even for  $D = 0.1$ , but it is not evident due to low  $M_t$ . Compressibility effects imply in the following discussion that we face a large magnitude of pressure fluctuations.

As we move away from the wall, fluctuations of both,  $p$  and  $\rho$ , decrease, but are not perfectly correlated anymore due to the growing temperature fluctuations. After a critical distance from the wall, pressure fluctuations continue to decrease; the density fluctuations reach a minimum at  $z = z_*$ . This local minimum of  $\rho_{\text{rms}} / \langle \rho \rangle_{A,t}$  exists when pressure and temperature fluctuations become comparable in magnitude. For the highest dissipation number  $D = 0.8$ , density fluctuations at  $z < z_*$  are driven by temperature fluctuations in contrast to  $z > z_*$ . One also notes that the location of the secondary maximum of  $\rho_{\text{rms}} / \langle \rho \rangle_{A,t}$  does not match the local maxima of  $T_{\text{rms}} / \langle T \rangle_{A,t}$ . This implies that pressure fluctuations, although not dominant, remain significant and thus compressibility effects too (Jones *et al.* 2022).

These features are absent for  $D = 0.1$  in panel (a). Thus there seems to exist a critical  $D$  where a transition to the compressibility-dominated convection regime exists that is qualitatively different to the OB or anelastic limits. In order to identify the critical  $D$ , we plot the maximum relative thermodynamic fluctuations with respect to  $D$  in figure 3(c). We find a  $D_{\text{crit}} \approx 0.65$  for the present  $(Ra, \epsilon)$ . For  $D < D_{\text{crit}}$ , maxima of density and temperature fluctuations dominate over those of the pressure fluctuations. As  $D$  increases, the maximum pressure fluctuations start to increase as well which is connected with increasing differences in the maxima of density and temperature fluctuations. For  $D \geq D_{\text{crit}}$ , the maxima of pressure and density fluctuations collapse and are larger than the one for the temperature fluctuations.

Clearly, there are multiple physical processes and thus scales at play near the top boundary at high  $D$ . This seems to be similar to the turbulent boundary layer with its inner and outer scales (Smits *et al.* 2011). The behaviour of density can be analyzed to demarcate various regimes inside the boundary layers in compressible convection. We thus introduce the following boundary layer scales: (1)  $\lambda_{T_{\text{max}}}$  as the distance between the top wall and the location of the local maximum of the relative temperature fluctuations. (2)  $\lambda_{\rho_{\text{max}}}$  as the distance between the top wall and the maximum of the relative density fluctuations. Note that in OB and even anelastic convection,  $\lambda_{T_{\text{max}}} = \lambda_{\rho_{\text{max}}}$  (Jones *et al.* 2022). Furthermore, (3)  $\lambda_{\rho_{\text{min}}}$  as the distance between the top wall and the location of the local minimum of the relative density fluctuations. This distance corresponds to the location where we start to observe significant compressibility effects. Finally, (4)  $\lambda_{\rho_{\text{max}}, T}$  as the distance between the top wall and the local maximum of the relative density fluctuations corresponding to the maximum of local temperature fluctuations.

Next, we display all 4 scales  $\lambda_X$  versus  $D$  in the inset of figure 3(c).  $\lambda_{T_{\text{max}}}$  increases with  $D$  which is consistent with the growth of the thermal boundary layer thickness at the top,  $\lambda^T$ , see figure 2(a). We see a sudden transition of  $\lambda_{\rho_{\text{max}}}$  at  $D_{\text{crit}} = 0.65$  indicating that the maximum for  $D > D_{\text{crit}}$  is at  $z = H$ . Note also that for  $D < 0.65$ ,  $\lambda_{\rho_{\text{max}}} = \lambda_{\rho_{\text{max}}, T}$ . Both scales increase with  $D$ , but start to deviate from  $\lambda^T$  at  $D < D_{\text{crit}} = 0.65$ . This deviation starts for  $D \geq 0.5$ ; it suggests that pressure fluctuations are important already, but not as dominant as discussed before. It might thus indicate that anelastic approximation is strictly speaking not applicable even for  $D \geq 0.5$ . Finally,  $\lambda_{\rho_{\text{min}}}$  starts from nearly zero at  $D = 0.1$  with negligible compressibility. With increasing dissipation number  $\lambda_{\rho_{\text{min}}}$  increases. This is a new top boundary layer regime induced by the increasing stratification. It is in line with an increase of  $\lambda_{T_{\text{max}}}$  and  $\lambda^T$ , see again the inset of figure 2(a). We discuss the implications of this sublayer for the turbulent heat transfer in the next section.

## 5. Stratification impact on turbulent heat transfer

A systematic increase of the level of stratification, controlled by  $D$ , at relatively small superadibaticity of  $\epsilon = 0.1$  has a significant impact on the normalized stress profiles as seen in figure 4. We show the variation of the normalized convective heat flux profiles  $J_c(z)$  in (a) and the normalized density-temperature correlation profiles  $J_\rho(z)$  in (b) for all 8 runs. They are qualitatively similar, but sign-flipped behaviour is observed for both second-order correlations in (a,b). An increasing sublayer with an average ‘‘anti-convection’’-behaviour, i.e., negative convective heat flux and positive density-temperature correlation can be detected. For  $z \lesssim 0.9$  both mean profiles correspond to unstable convection.

Next, we relate the depth of these stabilized regions to  $\lambda_{\rho_{\text{min}}}$  and thus to the regime transition at  $D = D_{\text{crit}}$ . We therefore define three further distances or scales: (1)  $\delta_{u_z T}$

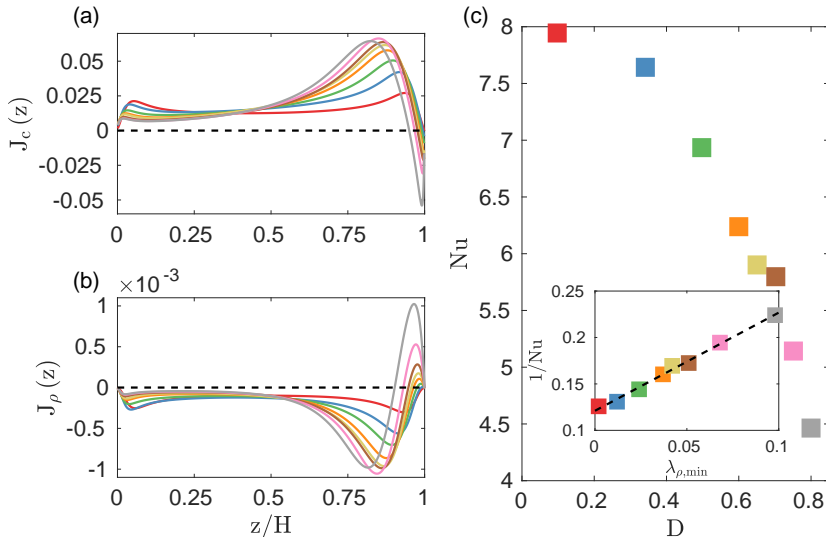


FIGURE 4. Profiles of plane-time averaged stresses versus  $D$ . (a) Normalized convective heat flux  $J_c(z) = \langle u'_z T' \rangle_{A,t} / [u_{z,\text{rms}}(z) \langle T(z) \rangle_{A,t}]$ . (b) Normalized density-temperature correlation  $J_\rho(z) = \langle \rho' T' \rangle_{A,t} / [\langle \rho(z) \rangle_{A,t} \langle T(z) \rangle_{A,t}]$ . (c) Nusselt number  $Nu$  versus dissipation number  $D$ , see eq. (5.1). Inset of (c) displays  $1/Nu$  versus  $\lambda_{\rho_{\min}}$ . The dashed line corresponds to a fit  $A + B\lambda_{\rho_{\min}}$  with coefficients  $A = 0.12$  and  $B = 1.05$ . Line colouring corresponds to table 1.

as the width of negative normalized heat flux with respect to the top boundary. (2)  $\lambda_{\rho' T'}^{\max}$  as the distance from the top boundary to the location of the positive maximum of the normalized density-temperature correlation. (3)  $\delta_{\rho' T'}$  as the width of the region of positive density-temperature correlations.

These length scales along with  $\lambda_{\rho_{\min}}$  are listed in table 1 for all DNS. We observe that for all runs, except for  $D = 0.1$ , the region of positive correlation exactly matches with the compressibility-dominated region, i.e.,  $\delta_{\rho' T'} = \lambda_{\rho_{\min}}$ . Thus, there is also a direct proportionality between regions dominated by compressibility and anti-convection with  $\delta_{u_z T} < \lambda_{\rho_{\min}}$ . For  $D \leq 0.70$ , we also find that  $\delta_{u_z T} \approx \lambda_{\rho' T'}^{\max}$ , the location of the maximum positive correlation. For  $D > 0.7$ , we get  $\delta_{u_z T} > \lambda_{\rho' T'}^{\max}$ , suggesting an increasing influence of compressibility. Furthermore,  $\delta_{u_z T} < \lambda_{\rho_{\min}}$  implies that on average weak convective motions can occur at heights,  $\lambda_{\rho_{\min}} \gtrsim z \gtrsim \delta_{u_z T}$ , even though there are already significant compressibility effects. We recall for this discussion that even for the highest  $D$ , we still observe focused cold thermal plumes which detach from the top thus indicating locally positive convective flux. All these processes take places in the region where density fluctuations are tightly correlated to pressure fluctuations as we discussed in figure 3(c). We also report that there is no trend of the location of maximum turbulent Mach number,  $M_t^* = \max_z M_t(z)$ , see figure 2(b), with  $D$  even though  $M_t^*$  increases with  $D$ . For all the cases considered, the distance of this maximum to the top wall is  $H - z_* \in [0.16, 0.174]$ , significantly larger than  $\lambda_{\rho_{\min}}$ . This again suggests the inadequacy of  $M_t$  alone to characterize general compressibility conditions (Donzis & John 2020). Particularly for the strongly asymmetric cases at highest  $D$ , the behaviour of compressible convection is completely different for same  $M_t$ -magnitude at either sides of  $z_*$ .

Finally, we plot the Nusselt number defined as

$$Nu = \frac{1}{2} \left[ -\frac{H}{\epsilon T_B} \frac{d\langle T_{sa} \rangle_{A,t}}{dz} \Big|_{z=0} + \frac{H}{\epsilon T_B} \frac{d\langle T_{sa} \rangle_{A,t}}{dz} \Big|_{z=H} \right] \quad (5.1)$$

with dissipation as function of  $D$  in figure 4(c). The Nusselt number is calculated as the average of the heat flux at the top and bottom. Since the flows are statistically steady, the Nusselt number at the top and bottom are the same and the maximum mean Nusselt number difference between the plate is found to be less than 3% for all cases. Clearly visible is that the Nusselt number  $Nu$  monotonically decreases with  $D$ . At critical  $D = 0.65$ , there seems to be slight change in behaviour but is not significant. To demonstrate conclusively that inefficient heat transfer is due to compressibility, we plot the inverse of the Nusselt number versus  $\lambda_{\rho_{\min}}$  in the inset of (c), we observe that the trend can be reasonably approximated by a linear fit.

## 6. Final discussion

The objective of the present study was to take the least complex, but fully compressible turbulent convection system to study the genuine effects of compressibility isolated from other major contributions to a non-Boussinesq behavior, such as temperature-dependent material properties, beyond the Oberbeck-Boussinesq and anelastic limits. We aimed at a configuration that is operated in the limit of strongly decreasing mean profiles of the thermodynamic state variables, the high stratification regime. It corresponds to the dissipation number of  $D \rightarrow 1$  for small superadiabaticity  $\epsilon$ . One prominent example for such a configuration might be the convection dynamics close to the solar surface. Even though the aim of our work is *not* to provide a realistic modeling of particularly this complex multi-physics flow and transport process, that involves the coupling to magnetic fields and radiation transfer, the present simulations provide an insight into generic physical mechanisms which lead to highly asymmetric thermal plume motions, the fundamental local process in any convection flow that triggers fluid turbulence and transports heat. The limit cases of our simplified configuration leads already to a sparse network of thin plume structures which resembles similarities to the granule network at the Sun, see again figure 1(b). These coherent structures “leak“ through the stratified top region and thus maintain a significantly reduced global turbulent heat transport. Future studies could aim at an increase of the aspect ratio and Rayleigh number together with a decrease of the Prandtl number and  $T$ -dependent material parameters.

## Acknowledgements

J.P.J. is supported by grant no. SCHU 1410/31-1 of the Deutsche Forschungsgemeinschaft and a Postdoctoral Fellowship of the Alexander von Humboldt Foundation. The authors gratefully acknowledge the Gauss Centre for Supercomputing e.V. (<https://www.gauss-centre.eu>) for funding this project by providing computing time through the John von Neumann Institute for Computing (NIC) on the GCS Supercomputer JUWELS at Jülich Supercomputing Centre (JSC).

The authors report no conflict of interest.

## REFERENCES

- ANDERS, E. H., LECOANET, D. & BROWN, B. P. 2019 Entropy rain: Dilution and compression of thermals in stratified domains. *Astrophys. J.* **884** (1), 65.

- BARANWAL, A., DONZIS, D. A. & BOWERSOX, R. D. W. 2022 Asymptotic behaviour at the wall in compressible turbulent channels. *J. Fluid. Mech.* **933**.
- BRANDENBURG, A. 2016 Stellar mixing length theory with entropy rain. *Astrophys. J.* **832** (1), 6.
- CHILLÀ, F. & SCHUMACHER, J. 2012 New perspectives in turbulent Rayleigh-Bénard convection. *Euro. Phys. J. E* **35** (7), 1–25.
- CHRISTENSEN-DALSGAARD, J. 2002 Helioseismology. *Rev. Mod. Phys.* **74** (4), 1073.
- COSSETTE, J.-F. & RAST, M. P. 2016 Supergranulation as the largest buoyantly driven convective scale of the Sun. *Astrophys. J. Lett.* **829** (1), L17.
- DONZIS, D. A. & JOHN, J. P. 2020 Universality and scaling in homogeneous compressible turbulence. *Phys. Rev. Fluids* **5**, 084609.
- HANASOGE, S. M., DUVALL JR, T. L. & SREENIVASAN, K. R 2012 Anomalously weak solar convection. *Proc. Nat. Acad. Sci.* **109** (30), 11928–11932.
- HANSON, C. S., DUVALL, T. L., BIRCH, A. C., GIZON, L. & SREENIVASAN, K. R 2020 Solar east-west flow correlations that persist for months at low latitudes are dominated by active region inflows. *Astro. & Astrophys.* **644**, A103.
- JEFFREYS, H. 1930 The instability of a compressible fluid heated below. In *Math. Proc. Camb. Phil. Soc.*, , vol. 26, pp. 170–172. Cambridge University Press.
- JOHN, J. P., DONZIS, D. A & SREENIVASAN, K. R 2019 Solenoidal scaling laws for compressible mixing. *Phys. Rev. Lett.* **123** (22), 224501.
- JOHN, J. P., DONZIS, D. A. & SREENIVASAN, K. R 2020 Compressibility effects on the scalar dissipation rate. *Combust. Sci. Technol.* **192** (7), 1320–1333.
- JOHN, J. P., DONZIS, D. A. & SREENIVASAN, K. R. 2021 Does dissipative anomaly hold for compressible turbulence? *J. Fluid. Mech.* **920**, A20.
- JOHN, J. P. & SCHUMACHER, J. 2023 Strongly superadiabatic and stratified limits of compressible convection. *arXiv preprint arXiv:2302.03621* .
- JONES, C. A., MIZERSKI, K. A & KESSAR, M. 2022 Fully developed anelastic convection with no-slip boundaries. *J. Fluid Mech.* **930**, A13.
- LELE, S. K. 1992 Compact finite-difference schemes with spectral-like resolution. *J. Comp. Phys.* **103**, 16–42.
- MAGIC, Z., COLLET, R., ASPLUND, M., TRAMPEDACH, R., HAYEK, W., CHIAVASSA, A., STEIN, R. F. & NORDLUND, Å. 2013 The Stagger-grid: A grid of 3D stellar atmosphere models–I. Methods and general properties. *Astro. & Astrophys.* **557**, A26.
- NORDLUND, Å., STEIN, R. F. & ASPLUND, M. 2009 Solar surface convection. *Living Rev. Solar Phys.* **6** (1), 1–117.
- OGURA, Y. & PHILLIPS, N. A. 1962 Scale analysis of deep and shallow convection in the atmosphere. *J. Atmos. Sci.* **19** (2), 173–179.
- RINCON, F. & RIEUTORD, M. 2018 The Sun’s supergranulation. *Living Rev. Solar Phys.* **15**, 1–74.
- SCHEEL, J. D. & SCHUMACHER, J. 2014 Local boundary layer scales in turbulent Rayleigh-Bénard convection. *J. Fluid. Mech.* **758**, 344–373.
- SCHUMACHER, J. & SREENIVASAN, K. R. 2020 Colloquium: Unusual dynamics of convection in the Sun. *Rev. Mod. Phys.* **92** (4), 041001.
- SMITS, A. J., MCKEON, B. J. & MARUSIC, I. 2011 High-Reynolds number wall turbulence. *Annu. Rev. Fluid Mech.* **43**, 353–375.
- VERHOEVEN, J., WIESEHÖFER, T. & STELLMACH, S. 2015 Anelastic versus fully compressible turbulent Rayleigh-Bénard convection. *Astrophys. J.* **805** (1), 62.